Progress in Oceanography 222 (2024) 103229

Contents lists available at ScienceDirect

Progress in Oceanography

journal homepage: www.elsevier.com/locate/pocean

Semidiurnal Internal Tides in a Shelf Sea South of Japan: Characteristics, Energetics, and Temporal variations

Shuya Wang [a], Xinyu Guo [a,*], Akihiko Morimoto [a], Anzhou Cao [b,a], Eisuke Tsutsumi [c], Yasumasa Miyazawa [d], Sergey M. Varlamov [d]

[a] Center for Marine Environmental Studies, Ehime University, Matsuyama, Japan
[b] Ocean College, Zhejiang University, Zhoushan, China
[c] Faculty of Fisheries, Kagoshima University, Kagoshima, Japan
[d] Application Laboratory, Japan Agency for Marine-Earth Science and Technology, Kanagawa, Japan

ARTICLE INFO

Keywords:
Internal tide
Bungo Channel
Temporal variation

ABSTRACT

Tidal mixing in a shelf sea south of Japan (Bungo Channel) plays an important role in modulating the water exchange between the Seto Inland Sea and Pacific Ocean. In this study, based on moored observations and model results from the Japan Coastal Ocean Predictability Experiment—Tides (JCOPE-T), the generation, propagation, and dissipation of semidiurnal internal tides in the Bungo Channel are investigated. Observational results indicate that semidiurnal internal tides induce strong baroclinic currents reaching 0.3 m/s. Their energy shows obvious spring-neap tidal cycles, generally coinciding with the local barotropic tidal forcing. By conducting the empirical orthogonal function analysis, we find that the observed semidiurnal internal tides are mainly dominated by the first two baroclinic modes. The JCOPE-T results suggest two main generation sites for semidiurnal internal tides in the region: one is located at a narrow strait north of the Bungo Channel, while the other is at the shelf break south of the Bungo Channel. The latter makes a major contribution to the observed semidiurnal internal tides. Northward internal tides generated at the shelf break are superposed with those generated at the narrow strait, causing a complex interference pattern in the channel. The temporal variation of semidiurnal internal tides in the Bungo Channel is affected by several factors. The intraseasonal variation of semidiurnal internal tides can be modulated by the Kuroshio warm water intrusion (*Kyucho*) because the occurrence of *Kyucho* changes the stratification in the channel and hence affects the energy conversion. The seasonal variation of semidiurnal internal tides in the Bungo Channel is determined mainly by the seasonally varying stratification; while those generated at the shelf break are under the combined influence of seasonal stratification and background currents. Southward internal tides from the shelf break are refracted due to the spatially varying stratification and background currents. The varying Kuroshio path and strength modulate the refraction of internal tides.

1. Introduction

Internal tides are a kind of internal waves with tidal frequencies, which induce isopycnal displacements of O(10–100) m in the ocean interior, with horizontal currents of O(0.1) m/s (Rudnick et al., 2003; Nash et al., 2006; Alford et al., 2011). When barotropic tidal currents flow over variable bottom topographies, they push the stratified seawater up and down over topographies, thereby generating internal tides (Garrett and Kunze, 2007). Internal tides are considered an intermediate step in the oceanic energy cascade. Globally, approximately 1 TW energy is converted from barotropic tides to internal tides and finally contributes to turbulent mixing via the breaking of internal tides (Simmons et al., 2004; Niwa and Hibiya, 2011; Müller, 2013). It is essential for the maintenance of global meridional overturning circulation (Munk and Wunsch, 1998; Nikurashin and Ferrari, 2013).

Marginal seas are regarded as hotspots for internal tides. Previous studies have indicated high energy conversion rates at the continental shelf break and slope where large gradients of water depth exist, such as in Biscay Bay (Gerkema et al., 2004), Monterey Bay (Kang and Fringer, 2012), the northern Bay of Bengal (Jithin et al., 2020), and Amazon

* Corresponding author.
E-mail address: guo.xinyu.mz@ehime-u.ac.jp (X. Guo).

https://doi.org/10.1016/j.pocean.2024.103229
Received 8 October 2023; Received in revised form 29 January 2024; Accepted 15 February 2024
Available online 17 February 2024

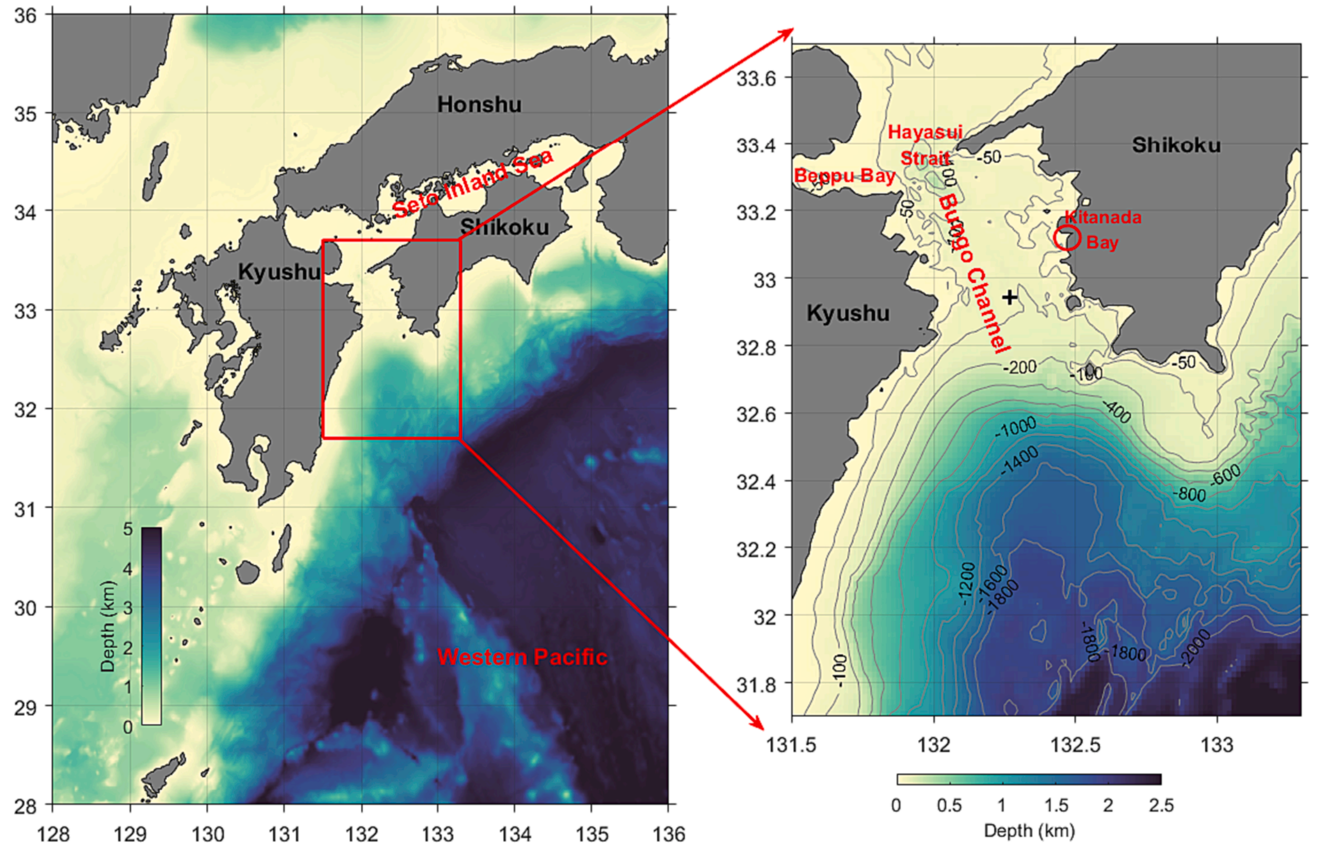

Fig. 1. (a) Bathymetry around the shelf seas west of Japan (shading, unit: km). The red rectangle indicates the study region. (b) Enlarged map for the Bungo Channel. The black plus indicates the location of moored ADCP. Gray contours in (b) denote isobaths in meters. (For interpretation of the references to color in this figure legend, the reader is referred to the web version of this article.)

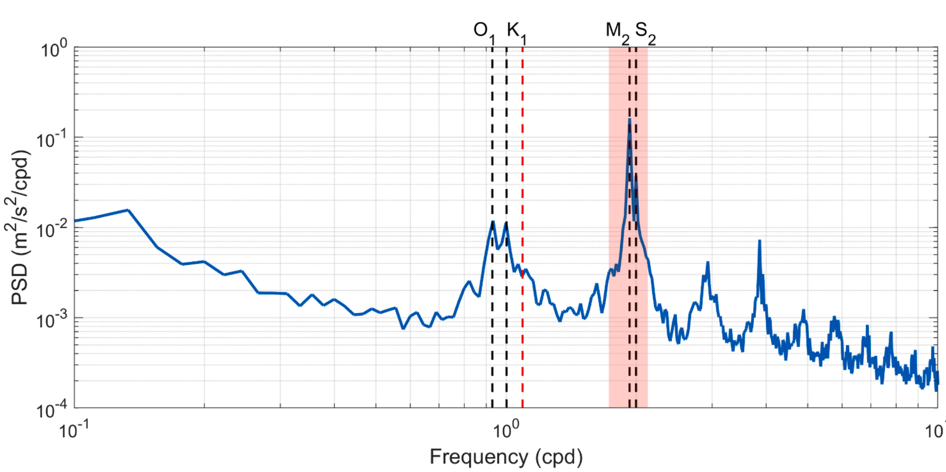

Fig. 2. Depth-averaged power spectrum for the observed baroclinic velocity. Tidal frequencies are indicated by black dashed lines and local Coriolis frequency is denoted by red dashed lines. Semidiurnal frequency band is denoted by red shading. (For interpretation of the references to color in this figure legend, the reader is referred to the web version of this article.)

Shelf (Tchilibou et al., 2022). Near the topography, the generated internal tides usually exhibit a beam-like structure due to the superposition of a series of vertical modes (Gerkema and Zimmerman, 2008). Because of the low wave speed and strong vertical shear, high modes are usually dissipated locally around the generation sites (Kelly et al., 2013); while low modes can be radiated offshore to the far field (Zhao et al., 2016; Jithin et al., 2019). Hence, the latter could affect the redistribution of energy in the ocean.

The breaking of internal tides in marginal seas leads to intensified turbulent mixing. Lien and Gregg (2001) reported that the energy dissipation rates exceeded 10^{-6} W/kg within the semidiurnal internal tidal beam in Monterey Bay. Nash et al. (2007) observed the bottom-enhanced diapycnal diffusivity induced by internal tides on the Oregon continental slope, with a magnitude of approximately 10^{-2} m^2/s. The mixing induced by internal tides further affects other processes in the shelf seas, e.g., the resuspension of sediments (Cacchione et al., 2002; Wang et al., 2020), nutrient transport (Xu et al., 2020), and underwater sound propagation (Duda et al., 2019).

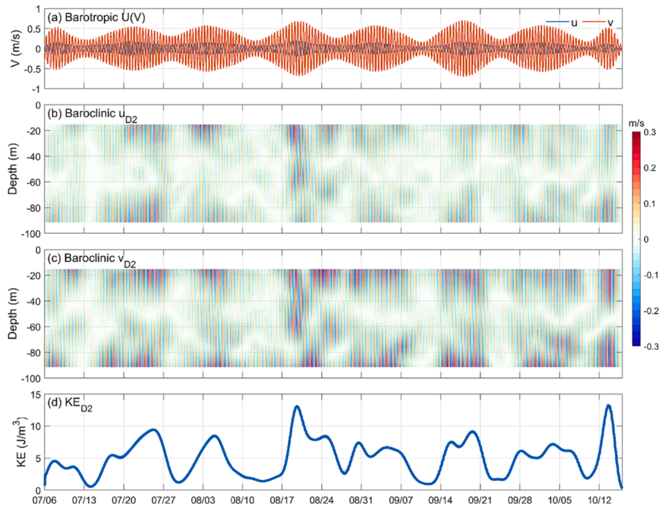

Fig. 3. (a) Semidiurnal barotropic velocity at the observational station. Depth-time map for (b) zonal and (c) meridional semidiurnal baroclinic velocities (shadings, unit: m/s). (d) Lowpassed depth-averaged kinetic energy of semidiurnal internal tides.

The Bungo Channel is located between the Kyushu and Shikoku Islands, which connects the Seto Inland Sea and the Pacific Ocean (Fig. 1a). The water depth in the channel varies from 60 to 100 m (Fig. 1b). The intrusion of Kuroshio warm water (*Kyucho*) into the Bungo Channel promotes the water exchange between the Pacific and this channel (Takeoka and Yoshimura, 1988; Kaneda et al., 2002; Isobe et al., 2010; Morimoto et al., 2022). It has been observed that the *Kyucho* exhibits an obvious spring-neap variation, which mainly occurs during the neap tide (Takeoka and Yoshimura, 1988; Takeoka et al., 1993). Further numerical studies indicate that the *Kyucho* is attributed to the temporal variation of tidal mixing. Namely, enhanced tidal mixing in the Bungo Channel during the spring tide could inhibit the northward intrusion of the Kuroshio; while weakened mixing during the neap tide enables the warm water to enter the channel (Nagai and Hibiya, 2012; 2013).

Internal tides are responsible for turbulent mixing in the Bungo Channel. Observational results by Kawamura et al. (2006) demonstrate strong semidiurnal internal tides associated with isotherm displacements over 10 m in the Kitanada Bay of the Bungo Channel, which could lead to shear instability near the bottom. However, further investigations on internal tides in the Bungo Channel have been rare over the past decade, leaving several questions that still need clarification: a) What are the characteristics of internal tides? b) Where are the internal tides generated and dissipated in this region? c) How do the internal tides vary temporally? To answer the above questions, we carry out this study.

In this study, the dominant internal tides – semidiurnal internal tides in the Bungo Channel are investigated by using moored observations and state of the art numerical model (Japan Coastal Ocean Predictability Experiment—Tides, JCOPE-T) output. The characteristics, energetics, and seasonal variations of semidiurnal internal tides are analyzed. This paper is organized as follows. The mooring data, JCOPE-T dataset, and corresponding processing methods are described in Section 2. Observational results are presented in Section 3. Energetics and seasonal variations of semidiurnal internal tides revealed by JCOPE-T results are shown in Section 4. Factors affecting the temporal variation of semidiurnal internal tides are discussed in Section 5. Finally, Section 6 summarizes this paper.

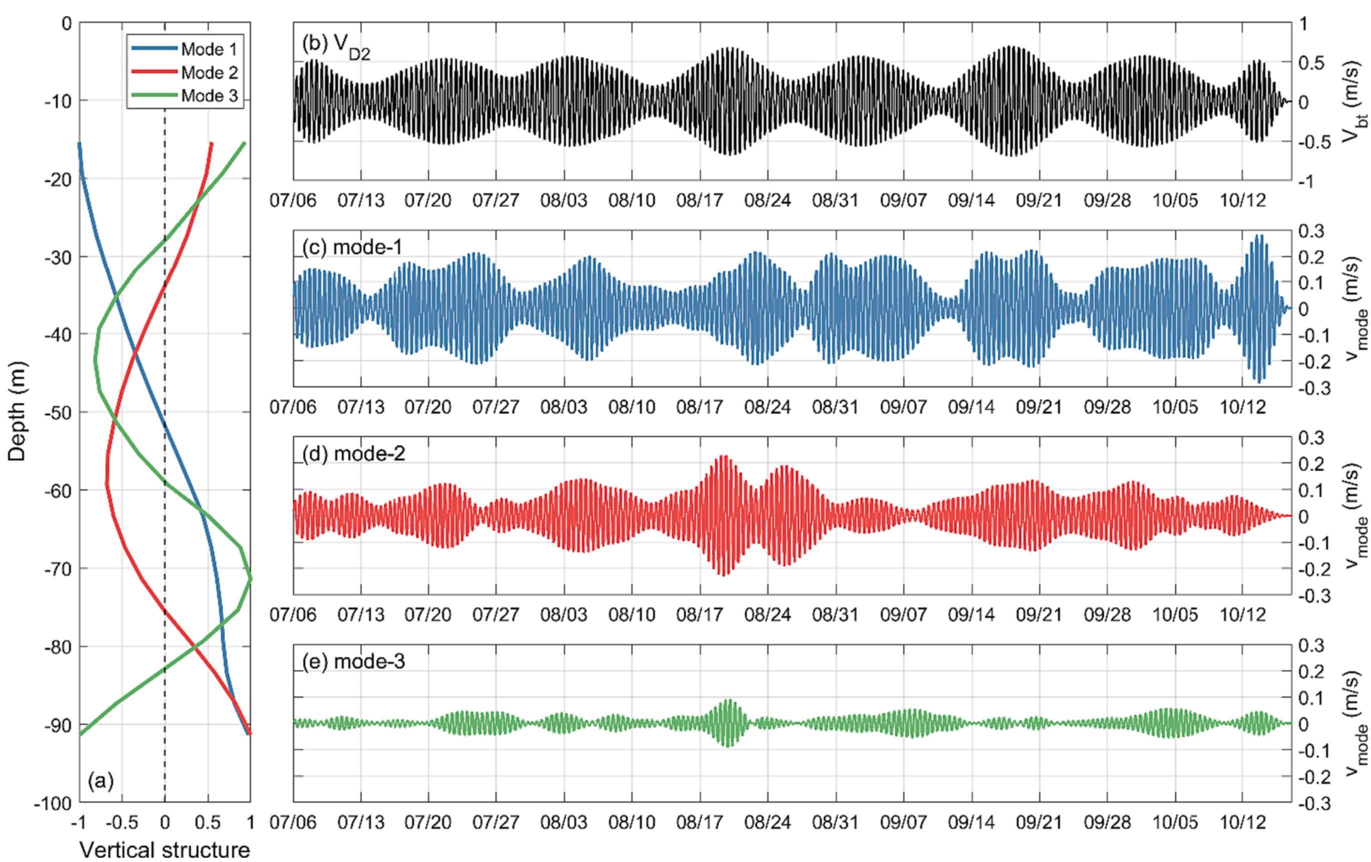

Fig. 4. Results for the EOF analysis on the meridional baroclinic velocities of semidiurnal internal tides. Vertical structures of the first three modes are shown in (a), while the principal components are shown in (c-e), respectively. Meridional semidiurnal barotropic velocity is plotted in (b) for comparison.

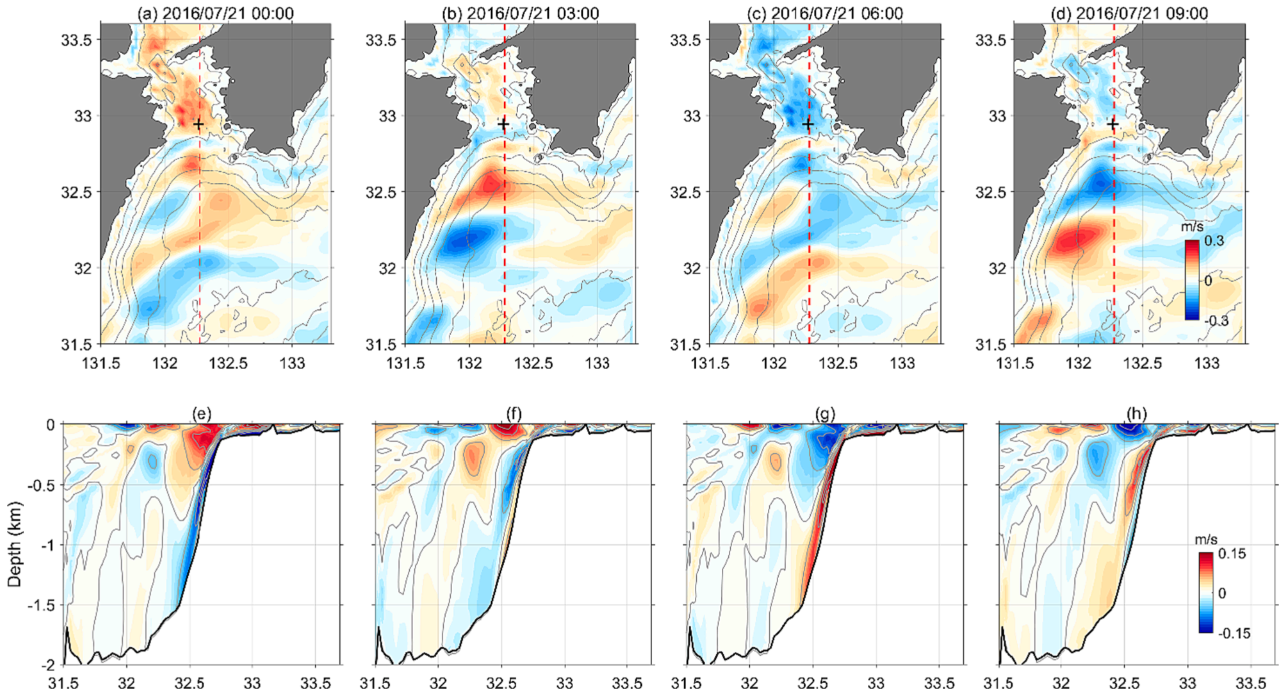

Fig. 5. (a-d) Snapshots of meridional components for semidiurnal baroclinic velocities (shadings, unit: m/s) at z = –10 m. Isobaths are denoted by gray contours. The observational station is indicated by the black plus. (e-h) Same as (a-d) but along the vertical transect marked by the red dashed line in (a-d). (For interpretation of the references to color in this figure legend, the reader is referred to the web version of this article.)

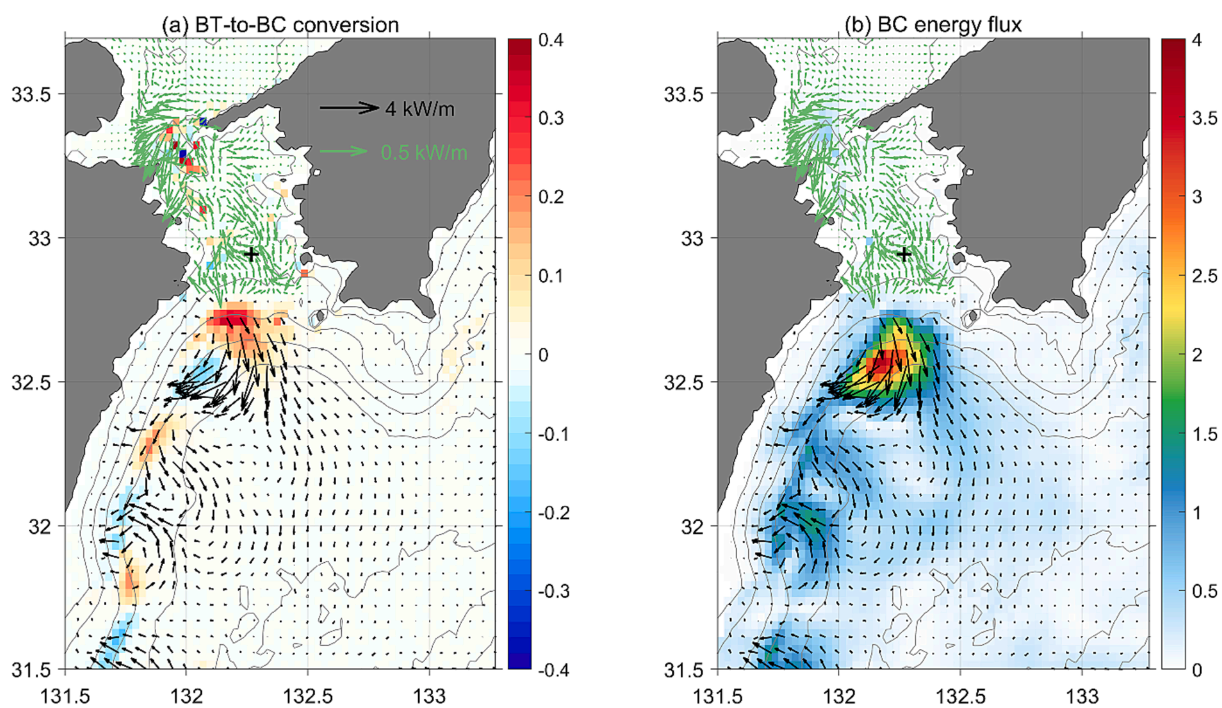

Fig. 6. (a) Depth-integrated barotropic-to-baroclinic energy conversion rate (shading, W/m^2) and (b) energy flux (shading, unit: kW/m) of semidiurnal internal tides. In each panel, vectors of energy flux are indicated by black and green arrows in different scales. Isobaths are denoted by gray contours, while the observational station is by the black plus. (For interpretation of the references to color in this figure legend, the reader is referred to the web version of this article.)

2. Data and methodology

2.1. Moored observations

An up-looking RDI 300 kHz acoustic Doppler current profiler (ADCP) was deployed in the Bungo Channel at (132.268°E, 32.942°N), where the water depth is 97.6 m (Fig. 1b). The ADCP has a sampling interval of 15 min and a vertical bin size of 4 m. It recorded currents from 2016/07/06 to 2016/10/17.

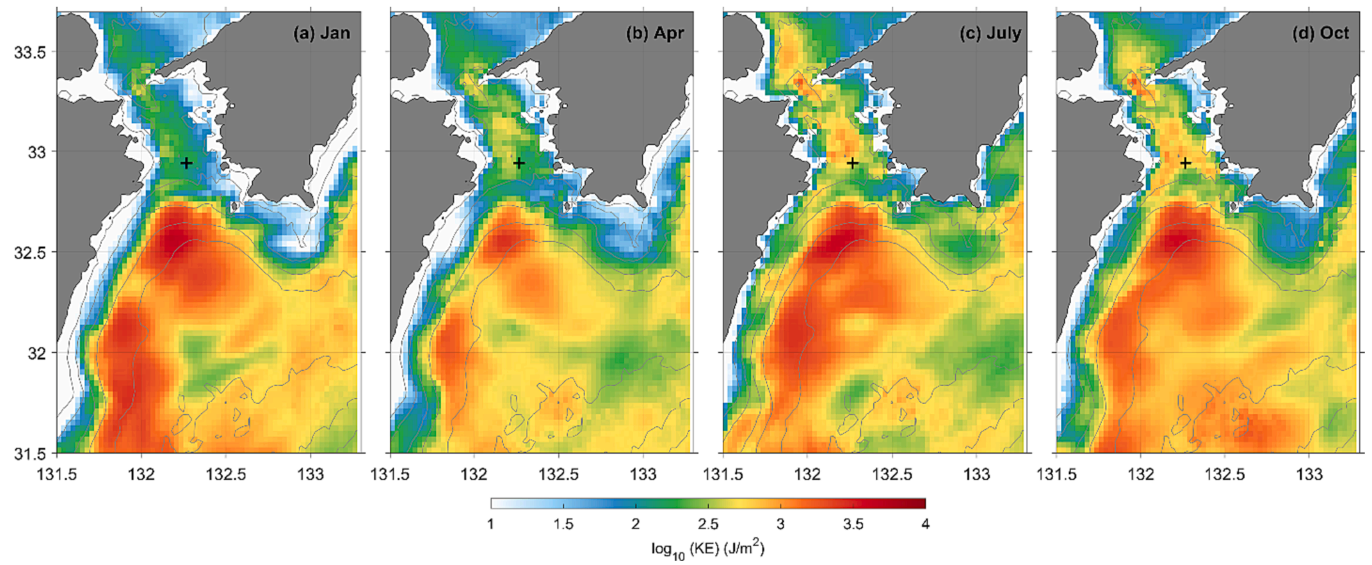

Fig. 7. Depth-integrated kinetic energy for semidiurnal internal tides (log form, shadings, unit: J/m^2) in (a) January, (b) April, (c) August, and (d) October. Isobaths are denoted by gray contours, while the observation site is by black plus.

2.2. JCOPE-T-NEDO

The JCOPE-T reanalysis data (JCOPE-T-NEDO) were produced by a tide-resolving ocean general circulation model JCOPE-T (Varlamov et al., 2015) for evaluating the energy potential of the ocean renewal energy around Japan (Waseda et al., 2016) with the support from New Energy and Industrial Technology Development Organization (NEDO). The model covers a horizontal range of 24°-48°N and 125°-148°E with a horizontal resolution of 1/36° and 46 vertical z-sigma levels from the surface to a depth of 6500 m. The surface momentum, heat, and salt (freshwater) fluxes are provided by bulk formulae (Li et al., 2010) with atmospheric variables from the National Centers for Environmental Prediction Climate Forecast System Reanalysis (CFSR, Saha et al., 2010) and Climate and Forecast System Version 2 (CFSv2, Saha et al., 2014). Lateral climatological monthly mean freshwater inputs from 47 major Japanese rivers are included in JCOPE-T. Observed features of geostrophic phenomena including the major ocean currents and mesoscale eddies are involved in JCOPE-T through a spectral nudging of temperature and salinity fields to those provided by the JCOPE2 reanalysis data (Miyazawa et al., 2009) with a relaxation time scale of five days. The model was run from the oceanic condition interpolated from the JCOPE2 data for a period from 2002 to the present with lateral boundary conditions calculated from the JCOPE2 data. The tidal forcing based on Oregon Tidal Inversion Software (Egbert and Erofeeva, 2002) is applied at the surface and lateral boundaries. The volume fluxes and sea level anomalies of 11 tidal constituents (Q_1, O_1, P_1, K_1, N_2, M_2, S_2, K_2, M_4, MS_4, MN_4) are provided at lateral boundaries. In addition, the surface pressure gradient included the equilibrium gradient induced by 25 potential tidal constituents: Q_1, O_1, M_1, P_1, K_1, J_1, OO_1, 2 N_2, MU_2, N_2, NU_2, M_2, L_2, T_2, S_2, K_2, M_4, MS_4, MN_4, MM, MF, SSA, SA, MTM, MSQM. The results of JCOPE-T are validated by comparison with observations (see Appendix).

2.3. Data processing

For ADCP data, the velocities in the upper 15 m are discarded due to many abnormal values. For the missing values in the remainder of the data, linear interpolation is used to fill in them in the temporal domain at each depth. The baroclinic velocity is obtained by removing the depth-averaged velocity from the raw velocity. Spectral analysis result indicates that semidiurnal signals are dominant in baroclinic motions since the corresponding peak values are basically one order of magnitude higher than those at diurnal frequencies (Fig. 2). That is why we focus on semidiurnal internal tides in this study. A fourth-order Butterworth filter is adopted to extract the baroclinic velocity of semidiurnal internal tides $\boldsymbol{u}'_{D2}$ as well as the semidiurnal barotropic velocity $\mathbf{U}_{D2}$, and the frequency band of [1.73 2.13] cpd is determined from the power spectrum. The kinetic energy of semidiurnal internal tides is calculated by

$$KE_{D2} = \frac{1}{2}\rho_0\left(u'^2_{D2} + v'^2_{D2}\right) \tag{1}$$

where $\rho_0 = 1025$ kg/m^3 is the reference density.

To explore the modal structure of semidiurnal internal tides, the empirical orthogonal function (EOF) method is considered, which is independent of any dynamical constraints. This method has been successfully used to clarify the dominant mode of internal tides in previous studies, which yields modal structures similar to those derived from the eigenvalue equation (e.g., Mackinnon and Gregg, 2003; Lee et al., 2012; Xu et al., 2013).

For the JCOPE-T data, the same filter as mentioned above is applied to the baroclinic velocity and pressure perturbation. The latter is calculated as,

$$p'(x,y,z,t) = \int_{-z}^{0}\rho'(x,y,\hat{z},t)g\,d\hat{z} - \frac{1}{H}\int_{-H}^{0}\int_{-z}^{0}\rho'(x,y,\hat{z},t)g\,d\hat{z}\,dz \tag{2}$$

where $\rho'(x, y, z, t)$ is the density perturbation calculated by subtracting the time-averaged density from the instantaneous density field (Nash et al., 2005), and $H(x, y)$ is the water depth. Then the energetics of semidiurnal internal tides are diagnosed by the following depth-integrated energy balance equation (Kerry et al., 2014),

$$\nabla_h \cdot \overline{\boldsymbol{F}_{D2}} = \overline{C_{D2}} - \overline{D_{D2}} \tag{3}$$

Terms in the equation denote divergence of baroclinic energy flux $\nabla\cdot\boldsymbol{F}_{D2}$, barotropic-to-baroclinic energy conversion rate C_{D2}, and energy dissipation rate D_{D2} corresponding to semidiurnal internal tides, respectively. The baroclinic energy flux and energy conversion rate are calculated by (Nash et al., 2005; Carter et al., 2008)

$$\overline{\boldsymbol{F}_{D2}} = \int_{-H}^{0}\boldsymbol{u}'_{D2}p'_{D2}\,dz \tag{4}$$

and

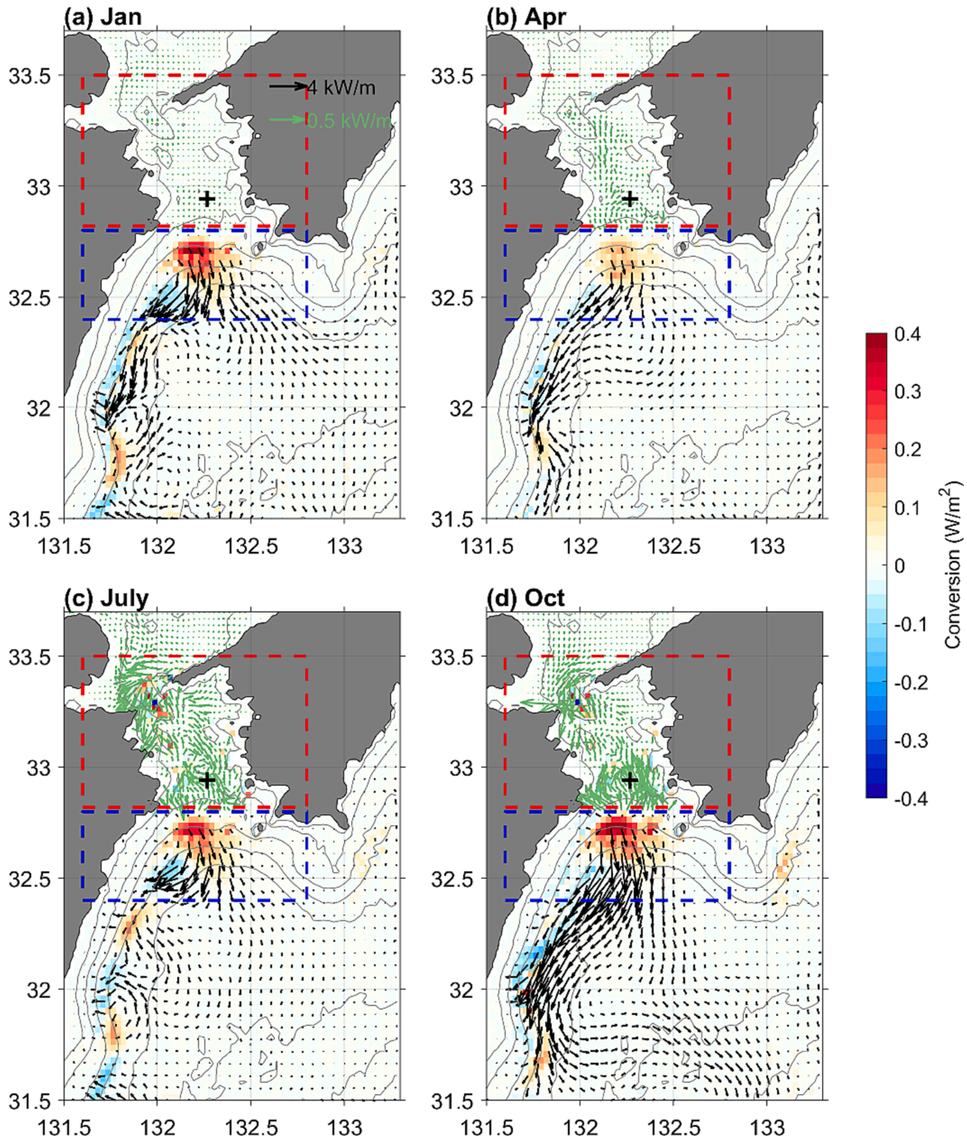

Fig. 8. Same as Fig. 6 but for barotropic-to-baroclinic energy conversion (shadings, unit: W/m^2) and energy flux (arrows, unit: kW/m). The red and blue dashed rectangles indicate the regions for integrating the energy conversion and dissipation in the Bungo Channel and shelf break, respectively. (For interpretation of the references to color in this figure legend, the reader is referred to the web version of this article.)

$$\overline{C_{D2}} = -(\boldsymbol{U}_{D2} \cdot \nabla H) p'_{D2}(z = -H) \quad (5)$$

The energy dissipation rate is obtained indirectly from Equation (3) as in previous studies (e.g., Alford et al., 2011; Kerry et al., 2014; Wang et al., 2021). Note that the calculated D_{D2} includes both the physical dissipation of internal tides and some biases caused by numerical dissipation and errors (Kang and Fringer, 2012).

3. Observational results

Observed semidiurnal barotropic and internal tides are shown in Fig. 3. In the Bungo Channel, the semidiurnal barotropic tidal currents are dominated by the meridional component. The magnitude exceeds 0.5 (0.3) m/s during the spring (neap) tide (Fig. 3a). In contrast, the zonal component only has a magnitude lower than 0.2 m/s even in the spring tide. The semidiurnal baroclinic velocities are weaker than the barotropic ones, which are also dominated by the meridional component (Fig. 3b-3c). The magnitude of v'_{d2} reaches 0.3 m/s during the spring tide but is lower than 0.1 m/s during neap tide (Fig. 3c). In addition, the semidiurnal baroclinic velocities are intensified near the surface and bottom, particularly during the spring tides. This preliminary result implies that the observed semidiurnal internal tides are largely dominated by mode-1.

The temporal variation of semidiurnal internal tides is indicated by their depth-averaged kinetic energy (Fig. 3d). It is easy to find that KE_{D2} exhibits a fortnight cycle, generally coinciding with the local semidiurnal barotropic tidal currents shown in Fig. 3a. Such consistency between KE_{D2} and V_{D2} indicates that the observed semidiurnal internal tides could be largely generated by local tidal forcing (Alford et al., 2011; Xu et al., 2014; Pickering et al., 2015; Cao et al., 2017). Moreover, during the observational period, there is no apparent seasonal variation of semidiurnal internal tides from summer to autumn, since the peak values of KE_{D2} basically keep a magnitude of 10 J/m^3 in each spring-neap cycle, except for that in the mid-October.

Then EOF method is applied to v'_{D2} to explore the modal structure of the semidiurnal internal tides. The first three modes are chosen because the sum of their variances accounts for 97 % of the total variance. Fig. 4a shows the vertical structures of the first three modes, which have been normalized by their maximum values. There appear 1, 2, and 3 cross-zero points for modes 1–3, respectively, suggesting that the EOF

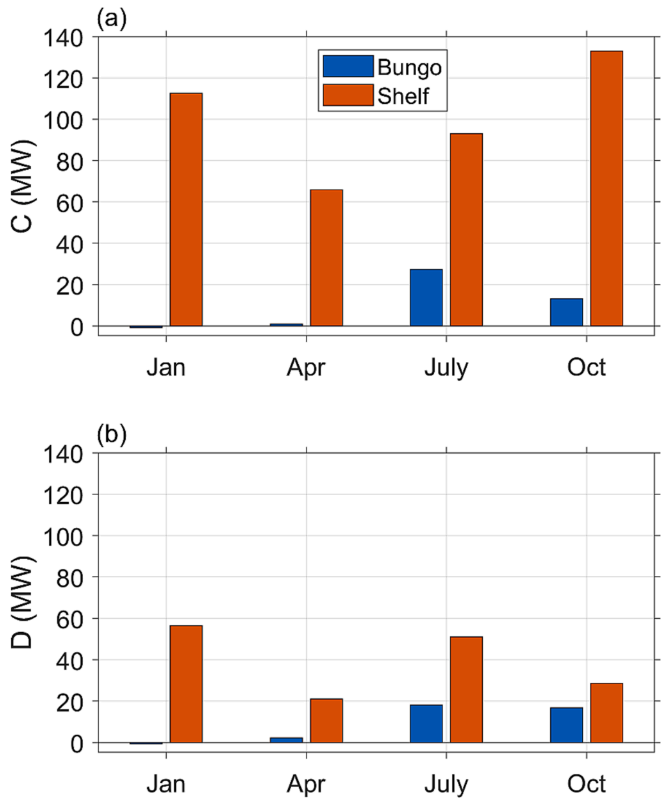

Fig. 9. Domain-integrated (a) barotropic-to-baroclinic energy conversion and (b) dissipation for the Bungo Channel (blue bars) and continental shelf south of the channel (red bars) in different months. (For interpretation of the references to color in this figure legend, the reader is referred to the web version of this article.)

modes correspond to the normal modes derived from the eigenvalue equation as in previous studies (Mackinnon and Gregg, 2003; Lee et al., 2012). We also use a one-month segment to conduct the EOF analysis, and the calculated vertical structures of modes show a similar pattern to those obtained with the data during the whole observational period (not shown). This suggests the temporal variation of vertical modal structure is not significant, agreeing with the results of Xu et al. (2013). Moreover, further sensitivity experiments with the JCOPE-T data at the observational station indicate that the lack of observations near the surface only has an influence on the vertical structures of higher modes (modes 2–3) rather than their principal components.

The contribution of each mode can be reflected by the principal components shown in Fig. 4c-4e. At the observational station, semidiurnal internal tides are dominated by modes 1 and 2 with magnitudes of 0.1–0.2 m/s. The former is stronger than the latter most of the time (Fig. 4c-4d). In contrast, mode-3 makes only a minor contribution as its magnitude is always lower than 0.05 m/s (Fig. 4e). A similar feature of semidiurnal internal tides has also been found in other shelf seas, such as the New England Shelf (Mackinnon and Gregg, 2003) and the Yellow Sea (Wang et al., 2020). Here, the temporal variation of mode-1 shows good consistency with the semidiurnal barotropic tidal current (Fig. 4b-4c). However, mode-2 is less correlated with the local tidal forcing when compared with mode-1, e.g., in late August and early September (Fig. 4d). Due to the low phase speed of high modes, their propagation is more easily affected by the varying background field (e.g., stratification and currents). As a result, they may become out of phase with the tidal forcing when reaching the observation station (Zhao et al., 2010).

4. JCOPE-T results

4.1. Spatial pattern and energetics of semidiurnal internal tides

Although semidiurnal internal tides have been observed in the Bungo Channel in a previous study (Kawamura et al., 2006) and this work, their spatial pattern and sources remain unclear because of the limitation of in-situ observations. Hence, we use JCOPE-T results to clarify the generation and propagation of semidiurnal internal tides in this region. Because the observation was conducted in the summer and autumn of 2016, in this section, we choose the JCOPE-T results in July 2016 for the corresponding investigation. As shown in Fig. 5a-5d, semidiurnal internal tides are observed to propagate southward into the deep Pacific Ocean from the continental slope south of the Bungo Channel. The generation of such offshore radiating waves is further illustrated by the vertical transects shown in Fig. 5e-5h, in which a beam radiated from the continental shelf break at 32.75°N is presented. Because the continental slope is supercritical (the topographic slope is larger than that of the internal tidal beam), there exists not only the dominant offshore propagating beam but also the weak onshore propagating one, agreeing with internal tide generation theory (Griffiths and Grimshaw, 2007; Gerkema and Zimmerman, 2008). With the increase of distance from the shelf break, the baroclinic velocity becomes weaker, indicating a quick decay of semidiurnal internal tides towards the Pacific Ocean.

In the Bungo Channel, the semidiurnal internal tides are weaker than those in the Pacific Ocean and exhibit complex features. First, the alternative pattern of positive and negative baroclinic velocities in the deep water is absent in the channel (Fig. 5a-5d). Second, the onshore radiating beam vanishes after reflection at the sea surface (Fig. 5e-5h). The above two factors make it difficult for us to determine the propagation direction of semidiurnal internal tides in the Bungo Channel.

Fig. 6a shows the spatial distribution of the energy conversion rate. Two regions with high C_{D2} are identified as main generation sites of internal tides in this region: one is located at the shelf break south of the Bungo Channel; while the other is at the Hayasui Strait north of the channel. For semidiurnal internal tides generated at the shelf break, a small fraction of their energy is radiated northward into the Bungo Channel, with energy fluxes of 0.2 kW/m. Because the observational station is near this generation site, most of the observed semidiurnal internal tides could be attributed to this source. This result further explains why the observed KE_{D2} is largely correlated with the local tidal forcing. In contrast, a large fraction of the internal tidal energy is radiated southward into the Pacific Ocean, with energy fluxes as high as 4 kW/m (Fig. 6b). Two branches of the offshore propagating beam are observed. The stronger one turns westward near the generation sites; while the weaker one directly propagates southward into the deep region. Moreover, the interaction between the former one and the continental slope east of Kyushu Island forms partially trapped slope waves, resulting in an alternative pattern of positive and negative energy conversion rates (Fig. 6a). A similar phenomenon has also been found over the Tasman Slope (Klymak et al., 2016).

At the Hayasui Strait, the presence of a strong barotropic tidal current and a large gradient of water depth caused by a depression is beneficial to the generation of internal tides. Although this generation site occupies a much smaller area, the conversion rates there are even higher than that at the shelf break. Near the Hayasui Strait, the semidiurnal energy fluxes have a magnitude of approximately 0.5 kW/m, which is larger than the northward ones radiated from the shelf break (Fig. 6b). However, most of the energy propagates westward into Beppu Bay or southwestward towards the coastal regions of Kyushu Island. Only a smaller fraction of energy is radiated southward into the Bungo Channel, and corresponding energy fluxes are comparable to the northward ones from the shelf break. The superposition of these semidiurnal internal tides and northward ones from the shelf break leads to a complex interference pattern in the Bungo Channel since there is no deterministic direction of energy flux (Fig. 6). This may explain why we

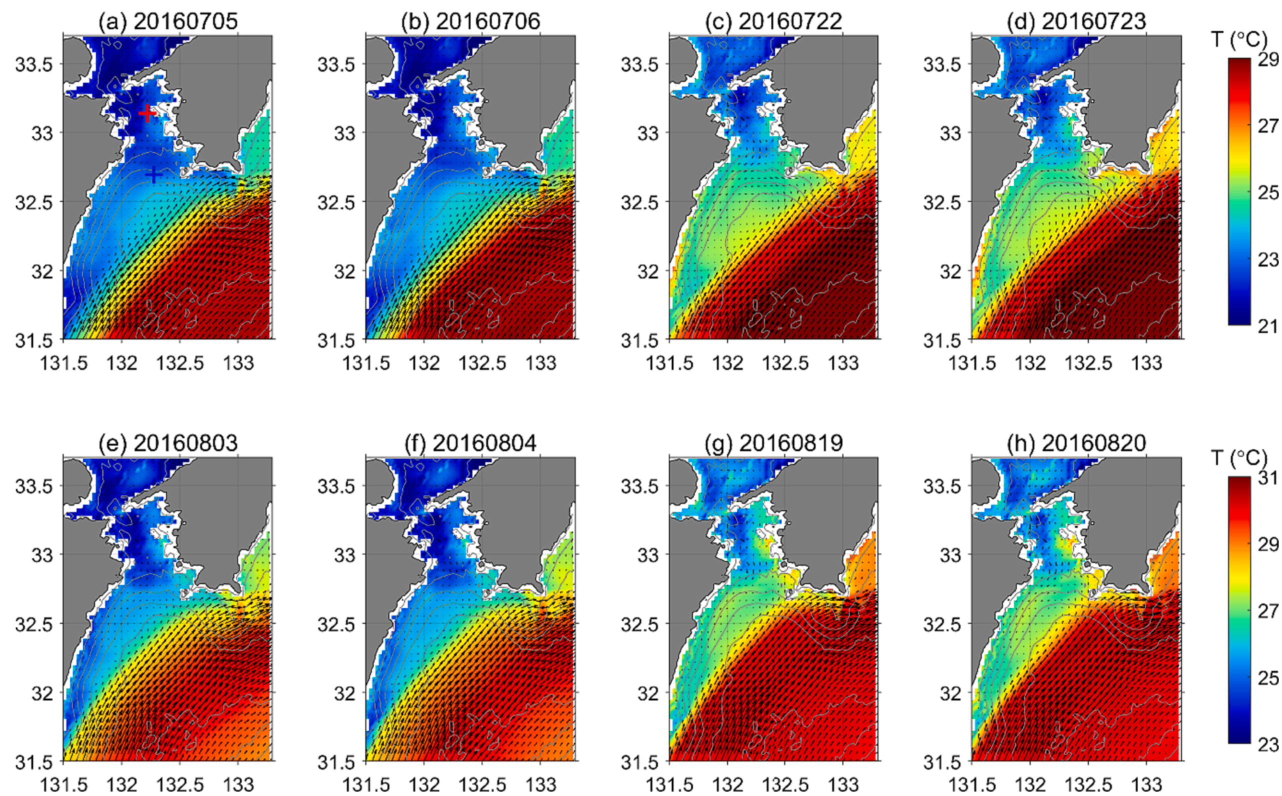

Fig. 10. Daily average temperature (shadings, unit: ℃) at z = –14 m and currents (arrows) from JCOPE-T results. In each panel, isobaths are indicated by gray contours. Blue and red pluses in (a) indicate the locations in the Bungo Channel and at the shelf break for analyses of barotropic tidal currents and stratification in Fig. 11. Note the different ranges of color bars for the upper and lower panels. (For interpretation of the references to color in this figure legend, the reader is referred to the web version of this article.)

cannot determine the propagation direction of internal tides directly from the wavefield (Fig. 5a-5d). This feature of internal tides has also been found in other shelf seas, such as the Yellow Sea (Liu et al., 2019) and the East China Sea (Lien et al., 2013). Additionally, although the observed semidiurnal internal tides are mainly generated at the shelf break, there also exist weak southward internal tides radiating from the Hayasui Strait. The latter may be out of phase with the local tidal forcing at the shelf break, hence causing the appearance of weak decorrelation between the observed KE_{D2} and local tidal forcing at some times during the observational period (Fig. 3, Kelly and Nash, 2010). Nevertheless, the long distance to the mooring site and weak energy flux implies that this source has only a limited contribution to the observed semidiurnal tides.

4.2. Seasonal variability

Because of the limited temporal range of moored observations, the whole seasonal cycle of semidiurnal internal tides cannot be determined. Therefore, JCOPE-T data are used for the corresponding investigation. Four months (January, April, July, and October) in 2016 are chosen to represent different seasons (winter, spring, summer, and autumn). Fig. 7 shows the depth-integrated KE_{D2}, which reflects the intensity of semidiurnal internal tides. It is easy to find that semidiurnal internal tides in the Bungo Channel exhibit an apparent seasonal cycle, which is weak in January and April (Fig. 7a-7b) but strong in July and October (Fig. 7c-7d). Their kinetic energy in July and October is nearly one order of magnitude higher than that in January and April. Also, semidiurnal internal tides in July and October do not show differences in their intensity (Fig. 7c-7d), agreeing with the observational results analyzed in Section 3. Around the shelf break, KE_{D2} does not show significant variation in different seasons. However, the spatial distribution of KE_{D2} varies in the deep region south of the continental shelf, implying that their propagation is modulated in different seasons.

In January and April, the energy conversion rate around the Hayasui Strait nearly approaches zero; and correspondingly, no energy radiation from the strait is observed (Fig. 8a-8b). In addition, the northward radiation of internal tidal energy from the shelf break into the Bungo Channel is also weak. Such lack of local generation and external energy input consequently results in weak semidiurnal internal tides in the Bungo Channel (Fig. 7a-7b). Differing from that at the Hayasui Strait, the internal tidal generation at the shelf break is not suppressed. Although the energy conversion there in April is weaker than that in January, a strong beam radiating southwestward along the coast of Kyushu Island appears in both seasons (Fig. 8a-8b).

However, the results for July and October exhibit a different pattern from those analyzed above. Internal tide generation at the Hayasui Strait is greatly enhanced, associated with higher energy conversion rates of over 0.4 W/m^2 and larger energy fluxes of about 0.5 kW/m (Fig. 8c and 8d). Also, northward energy fluxes from the shelf break into the Bungo channel are much larger than those in July and October. This is why intense semidiurnal internal tides are found in the two months as mentioned before. At the shelf break, energy conversion becomes slightly larger in October, accompanied by the strongest beam radiating southeastward among the four seasons.

Another interesting phenomenon is that the radiation of semidiurnal internal tides towards the deep Pacific Ocean exhibits varying patterns in different seasons. For the southwestward branch, it travels a long distance along the coast of Kyushu Island towards the Pacific Ocean in April and October (Fig. 8b and 8d); but decays quickly near the generation sites in July (Fig. 8c). The weak southward branch is more easily refracted and hence changes its direction, which even forms a loop-like structure in energy flux in January (Fig. 8b).

Energy conversion and dissipation of semidiurnal internal tides in the Bungo Channel and shelf break south of the channel are integrated to

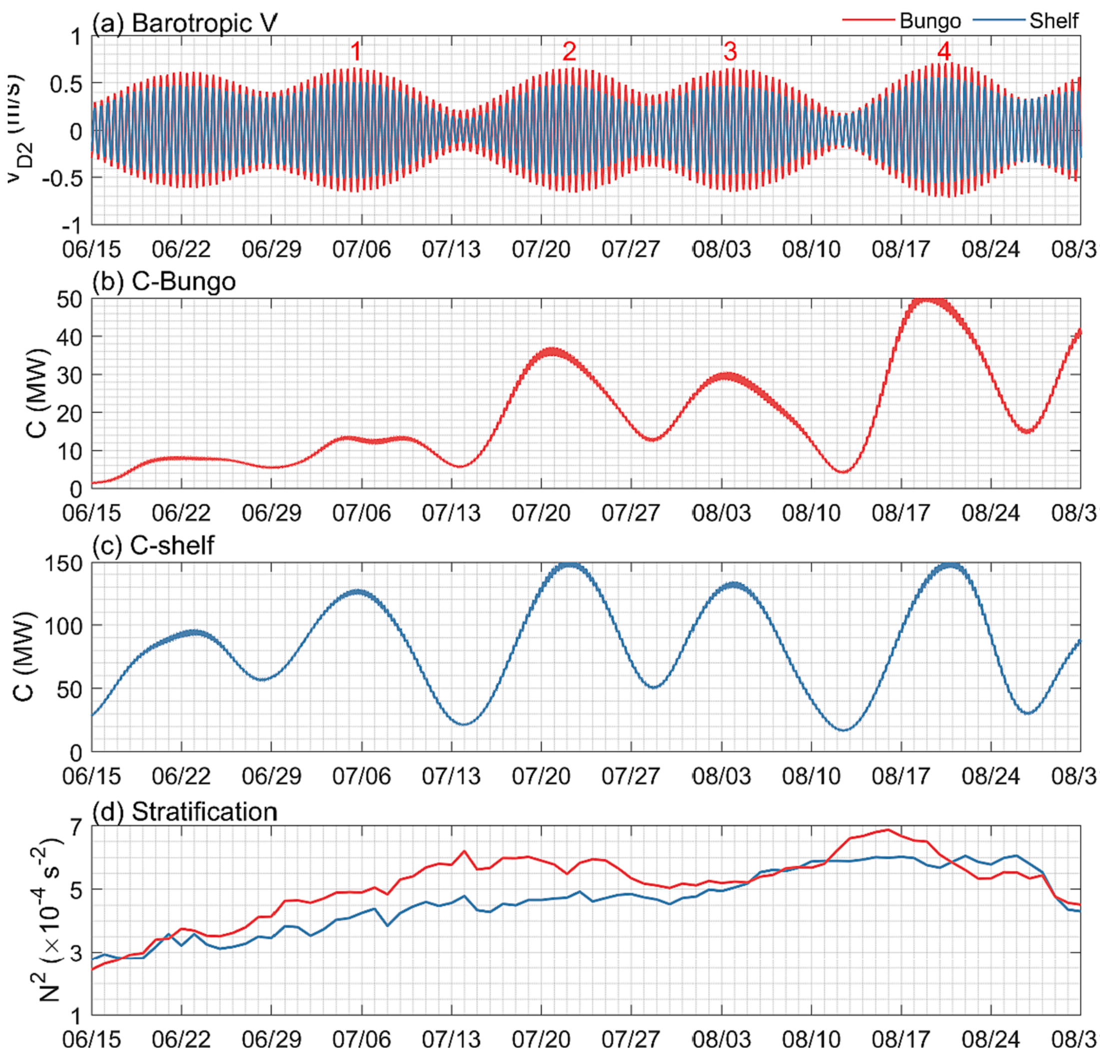

Fig. 11. (a) Semidiurnal meridional barotropic tidal currents at the shelf break (blue curve) and in the Bungo Channel (red curve) from 2016/06/15–2016/08/31. Note that the tidal current at the shelf break is enlarged by a factor of 5 for better comparison. The four stages of spring tides are denoted by colored numbers. Integrated energy conversion of semidiurnal internal tides (b) at the shelf break and (c) in the Bungo Channel. Note that the results are smoothed with a 25-h running average to remove high-frequency variation. (d) Depth-averaged stratification within the upper 60 m at the shelf break (blue curve) and in the Bungo Channel (red curve). (For interpretation of the references to color in this figure legend, the reader is referred to the web version of this article.). (For interpretation of the references to color in this figure legend, the reader is referred to the web version of this article.)

further illustrate their seasonal variations (Fig. 9). On the whole, the integrated semidiurnal energy conversion in the Bungo Channel is much lower than that at the shelf break (Fig. 9a). In the Bungo Channel, the total energy converted into semidiurnal internal tides is nearly zero in January and April but exceeds 25 MW in July. However, at the shelf break, semidiurnal internal tides exhibit a different seasonal cycle. Their generation is strongest in October but weakest in April, since the total energy conversion in October is almost twice as large as that in April. Moreover, the energy conversion in January and July is basically comparable, which is about 20 % lower than that in October.

The energy dissipation of semidiurnal internal tides in the Bungo Channel shares a similar seasonal cycle with the energy conversion (Fig. 9b), which is also intensified in July and October. Here, the dissipated energy is comparable to or even larger than locally converted energy from barotropic tides due to external energy input from the shelf break, implying that the Bungo Channel could be an energy sink of internal tides. In contrast, the energy dissipation around the shelf break is not strictly correlated with the energy conversion, as internal tidal energy dissipated in January and April is generally comparable despite the large difference in energy conversion in the two months (Fig. 9b). In addition, note that only half of the energy is dissipated locally at the shelf break, while the remainder is radiated into the Pacific Ocean, especially in October (Fig. 8d and 9b).

5. Discussion

5.1. Influence of *Kyucho*

The *Kyucho* usually occurs in summer and exhibits short-term temporal variation (Takeoka and Yoshimura, 1988; Takeoka et al., 1993; Isobe et al., 2010). Here, the influence of the *Kyucho* on the semidiurnal internal tides in the study region is explored. Fig. 10 shows the daily averaged temperature at z = –14 m, and the variations of energy conversion of semidiurnal internal tides are presented in Fig. 11. During the four spring tides (stages 1–4 in Fig. 11a) in July and August, the barotropic tidal currents are comparable in strength. However, the integrated energy conversion in the Bungo Channel shows large differences in the four stages (Fig. 11b). In contrast, the energy conversion integrated at the shelf break does not change considerably during the four spring tides (Fig. 11c).

Such modulation on the spring-neap cycle of semidiurnal internal tides could be attributed to the *Kyucho*. During stage 1, the *Kyucho* did

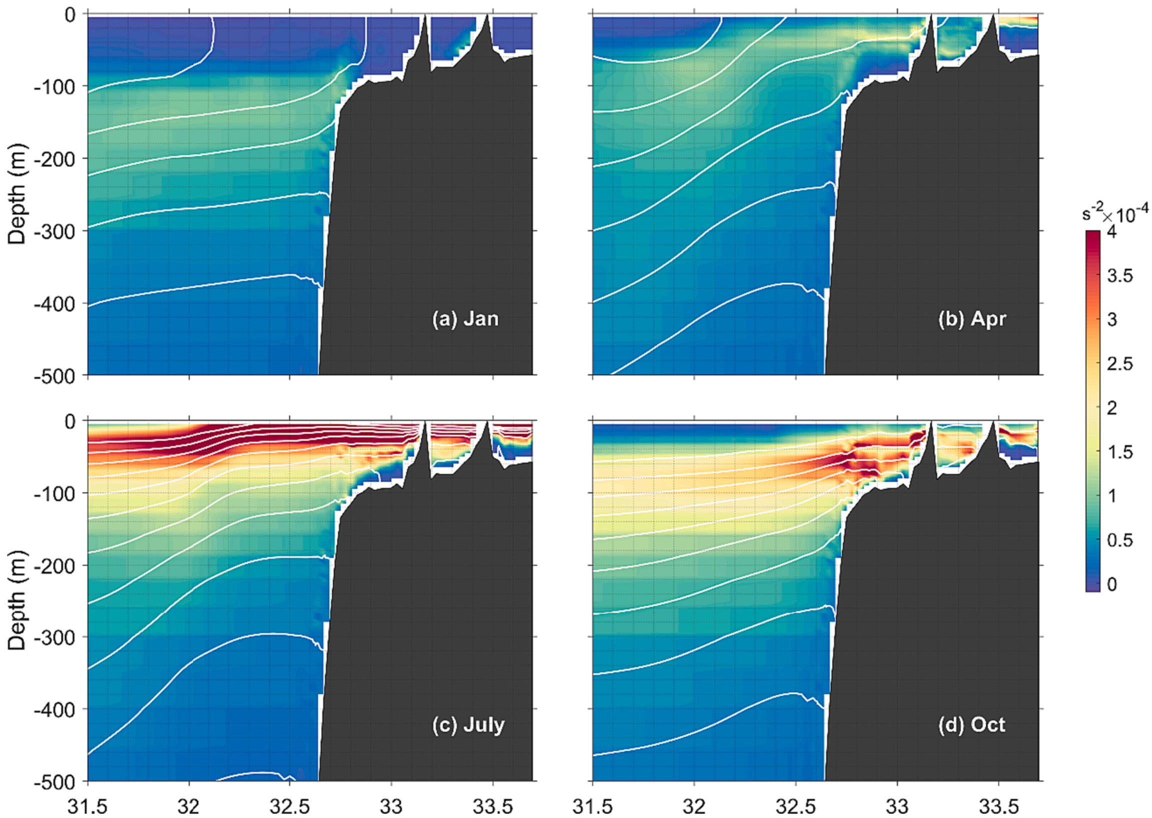

Fig. 12. Monthly-averaged squared buoyancy frequency (shadings, unit: s^{-2}) along the vertical transect denoted by red dashed line in Fig. 5a-5d. (For interpretation of the references to color in this figure legend, the reader is referred to the web version of this article.). (For interpretation of the references to color in this figure legend, the reader is referred to the web version of this article.)

not occur; and the water temperature in the Bungo Channel is nearly 5°C lower than that of the warm Kuroshio water in the Pacific Ocean (Fig. 10a-10b). In this situation, the squared buoyancy frequencies at the shelf break and in the Bungo Channel are basically equal (Fig. 11d). Whereas, the warm Kuroshio water intruded into the Bungo Channel on July 22, causing a significant increase in water temperature in the Bungo Channel on July 23 (Fig. 10c-10d). Correspondingly, the stratification in the Bungo Channel is greatly intensified during stage 2 when compared with that at the shelf break (Fig. 11d), resulting in the enhancement of energy conversion (Fig. 11b). In August, a similar event was found; i.e., the intrusion of warm water during stage 4 led to the intensification of stratification once again. This could explain the obvious difference in energy conversion in stages 3 and 4. The above results indicate that the *Kyucho* influences the short-term (intraseasonal) variation of semidiurnal internal tides by changing the local stratification. Note that a similar phenomenon was also observed by Kawamura et al. (2006), who revealed occasional enhancement of semidiurnal internal tides in the Bungo Channel affected by the *Kyucho*.

5.2. Influence of seasonal stratification

In shelf seas, the stratification usually exhibits more significant seasonal variation than that in the open ocean because of the shallow water depth (e.g., Chang et al., 2009; Tsutsumi and Guo, 2016; Yu and Guo, 2018). As a result, it can lead to seasonal variation of internal tides. We calculate the squared buoyancy frequency using the JCOPE-T data. Here, the seawater in the Bungo Channel is well mixed in January and April (Fig. 12a-12b). Such weak stratification cannot support the existence of internal tides. This explains why semidiurnal internal tides in the Bungo Channel are weak during that period (Figs. 7 and 9). In contrast, stratified seawater exists around the shelf break and in the Pacific Ocean throughout the year. Therefore, internal tides are always generated there and have a smaller seasonal variation than that in the Bungo Channel. Based on the above results, we can conclude that the seasonal variation of stratification in the Bungo Channel is the cause of the seasonal variation of semidiurnal internal tides.

Tsutsumi and Guo (2016) analyzed the water temperature data in the Seto Inland Sea, the Bungo, and Kii Channels, and found that the seasonal heat content in the upper ocean is larger determined by air-sea heat flux. This implies that the seasonally varying stratification in the Bungo Channel could be mainly controlled by surface heating and cooling, which further influences the seasonal variation of semidiurnal internal tides. At the shelf break, although the stratification shows a similar seasonal cycle to that in the Bungo Channel, the coastal circulation also varies in different seasons (Isobe et al., 2010), which affects the generation of internal tides (Masunaga et al., 2018).

5.3. Refraction of internal tides

As the semidiurnal internal tides generated at the shelf break propagate southward into the Pacific Ocean, they are refracted and therefore exhibit different radiation patterns (Fig. 8). For investigating the refraction of internal tides, we use the following wave front tracing model (Park and Watts, 2006; Park and Farmer, 2013)

$$\Delta d = C_p \Delta t \tag{6}$$

where Δd is the traveling distance of wave front in one time step Δt, and C_p is the phase speed calculated by

$$C_p = \frac{\omega}{\sqrt{\omega^2 - f^2}} C_n \tag{7}$$

Here, we use the M_2 tidal frequency $\omega = 1.405 \times 10^{-4}\ s^{-1}$. The eigenspeed C_n is obtained by solving the Sturm–Liouville equation (Gill,

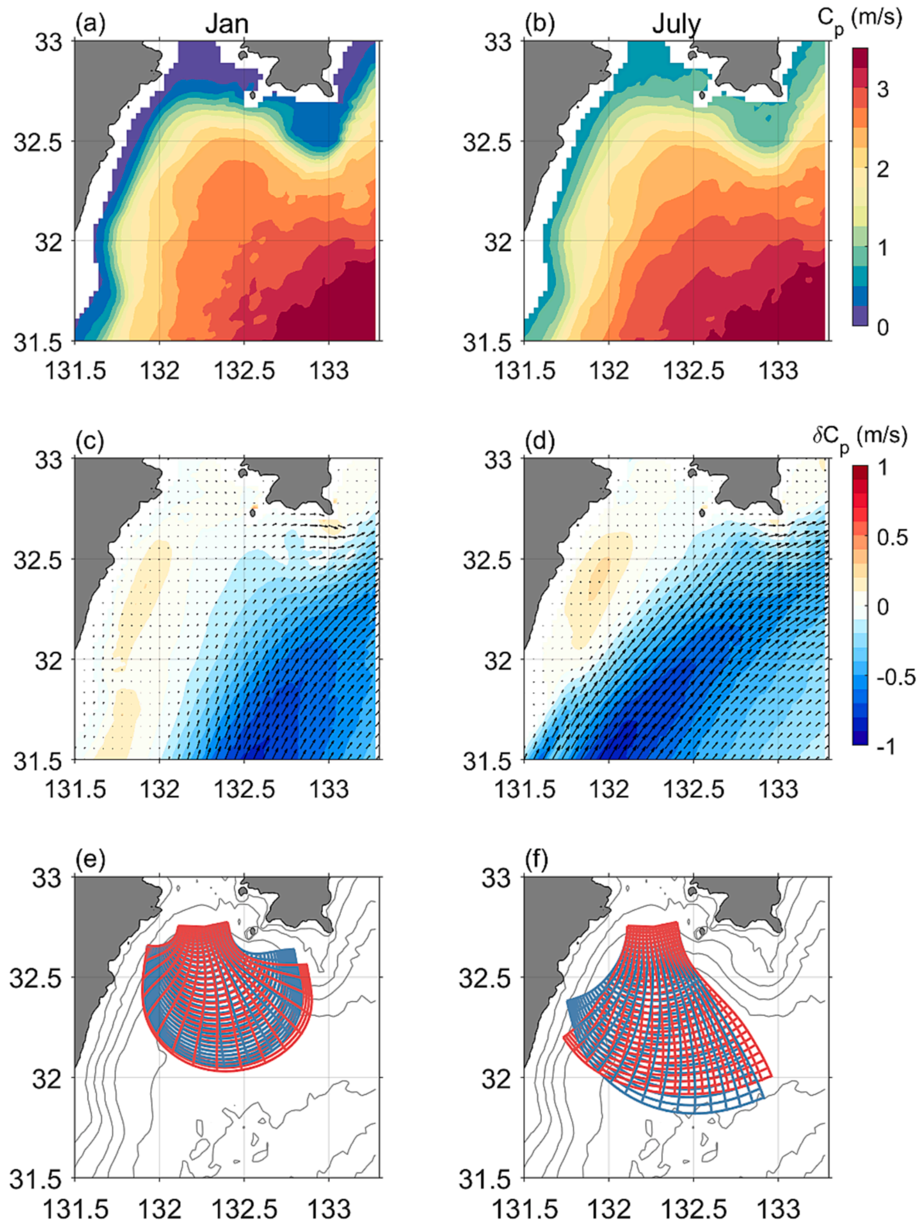

Fig. 13. (a and b) Phase speed obtained by solving Equations (7) and (8) (shadings, unit: m/s). (c and d) Difference between the phase speeds without and with background currents (shadings, unit: m/s). Black arrows denote surface currents. (e and f) Results for wave front tracing excluding (blue lines) and including background currents (red lines), respectively. Bathymetry is indicated by gray contours. (For interpretation of the references to color in this figure legend, the reader is referred to the web version of this article.)

1982)

$$W(z)_{zz} + \frac{N^2(z)}{C_n^2} W(z) = 0 \tag{8}$$

with monthly averaged stratification from JCOPE-T, where W(z) is the eigenfunction. Note that the effect of background currents is not considered in Equation (8). For waves propagating in background currents, the eigenspeed is calculated with the Taylor-Goldstein equation (Kundu and Cohen, 2002)

$$W(z)_{zz} - \frac{U(z)_{zz}}{U(z) - C_n} W(z) + \frac{N^2(z)}{[U(z) - C_n]^2} W(z) = 0 \tag{9}$$

Note that this model does not consider the anisotropic wavenumbers (the difference between the phase propagation direction and the ray direction). Hence, it cannot fully simulate the blocking of rays (loop-like pattern) by background currents as Duda et al. (2018).

Fig. 13 shows the results calculated by the wave front tracing model. It is easy to find that the Kuroshio path considerably affects the refraction of southward semidiurnal internal tides. As the Kuroshio axis is far from the shelf (Fig. 13c), the wave front is broadened quickly as the internal tides propagate southward from the continental shelf break (Fig. 13e). This result generally agrees with that shown in Fig. 8a, since the energy fluxes are divergent around the shelf break, despite the different intensities of the southwestward and southeastward beams. In addition, the results with and without background currents only show slight differences near the coast of Shikoku Island. This implies a weak effect of background currents on the propagation of internal tides, as the Kuroshio axis is a bit far from the continental slope (Fig. 13a and 13c). When the Kuroshio axis becomes close to the shelf, the calculated wave front shows an obviously different pattern (Fig. 13f), which could be largely due to the different spatial distribution of eigenspeed controlled

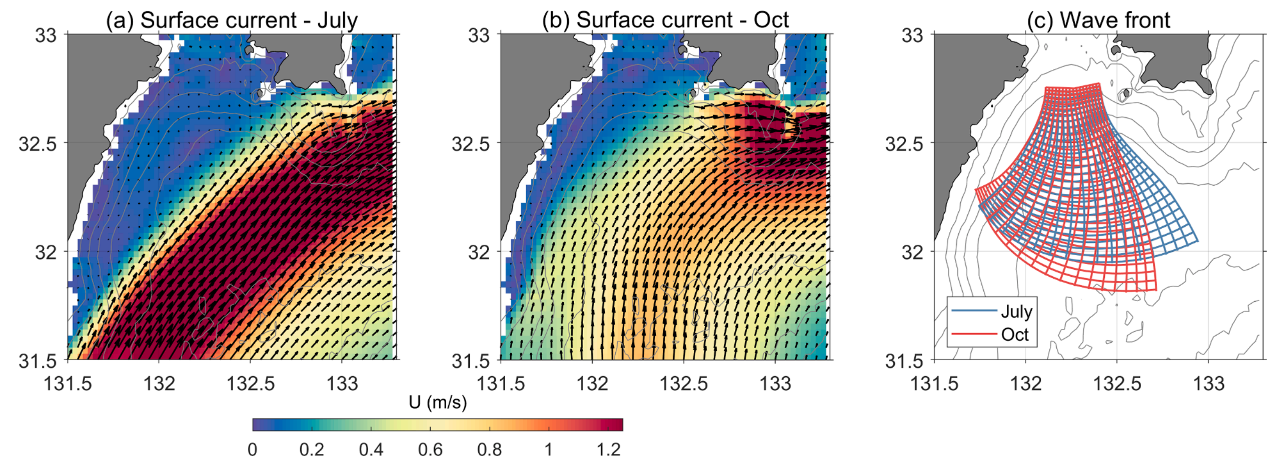

Fig. 14. Monthly-averaged surface currents in (a) July and (b) October, with magnitude indicated by shadings (unit: m/s) and directions by black arrows. (c) Results of wave front tracing model using the background field in summer (blue curves) and autumn (red curves). (For interpretation of the references to color in this figure legend, the reader is referred to the web version of this article.)

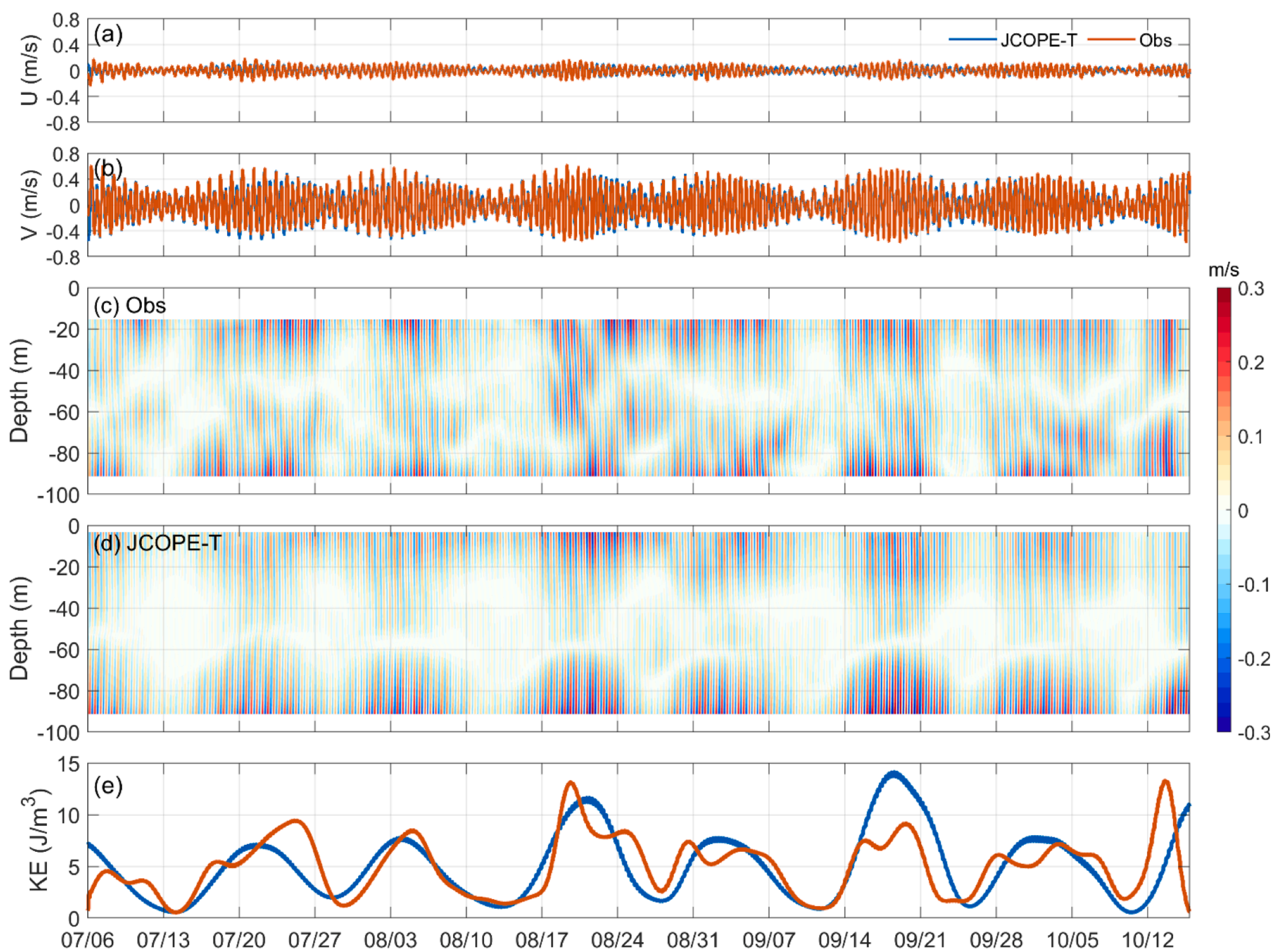

Figure A1. (a) Zonal and (b) meridional barotropic tidal currents at the moored ADCP station from JCOPE-T (blue curves) and observations (red curves). Meridional components of semidiurnal baroclinic velocity (shadings, unit: m/s) from (c) observations and (d) JCOPE-T results. (e) Depth-averaged kinetic energy for semidiurnal internal tides derived from JCOPE-T results (blue curve) and observations (red curve).

by background stratification (Fig. 13b). On the eastern side, the waves propagate almost southward into the Kuroshio region rather than turning eastward. Correspondingly, southward energy fluxes in the Kuroshio region are found in Fig. 8c, which confirms the wave front tracing results. Moreover, the semidiurnal internal tides are refracted more eastward when the background currents are considered in the calculation. The effect of background currents on the propagation of internal tides gradually becomes stronger as the semidiurnal internal tides are radiated away from the shelf break to the Kuroshio region.

In addition to the Kuroshio axis, the Kuroshio strength also

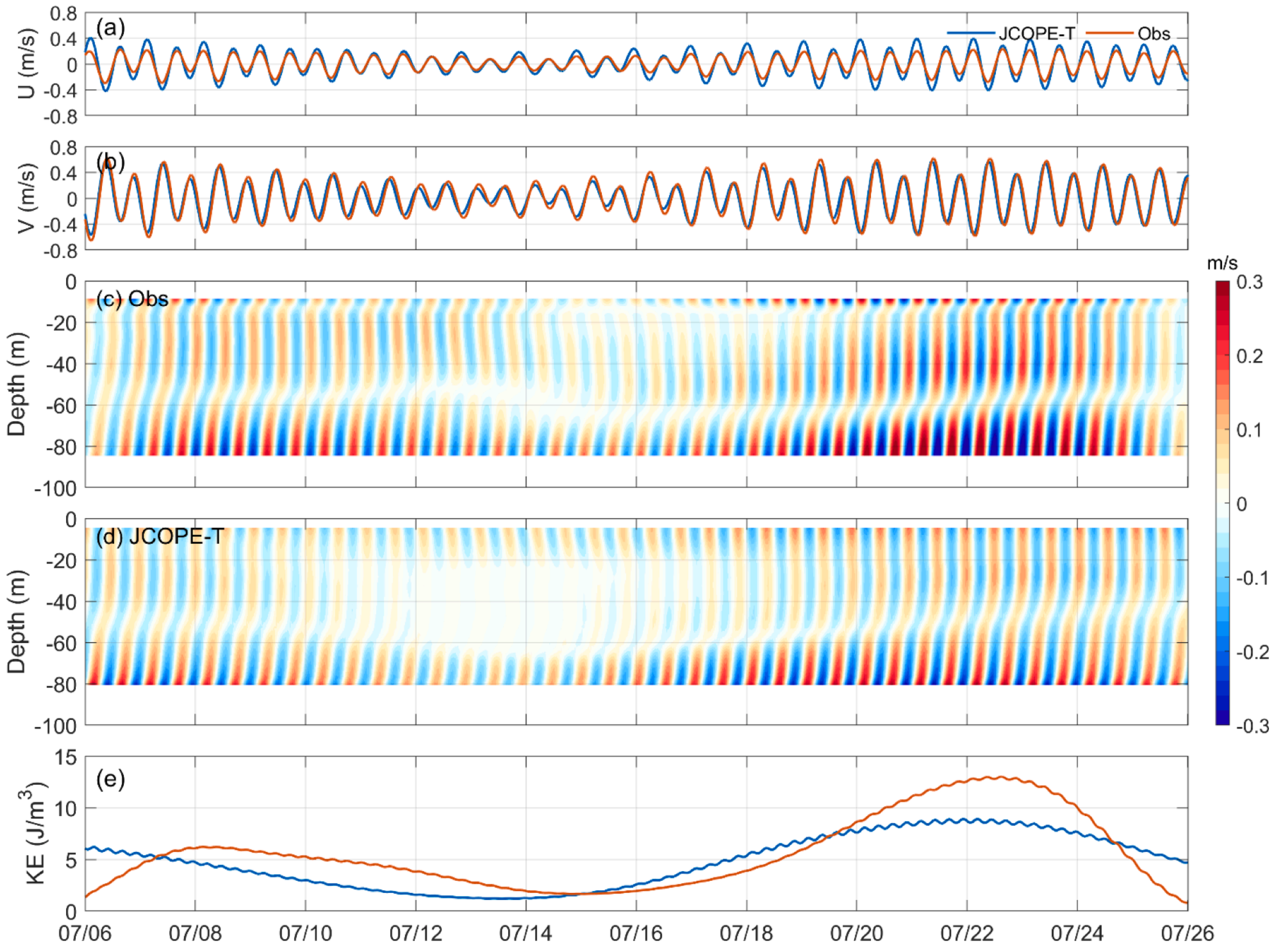

Figure A2. Same as Fig. A1 but for comparison with ADCP observations at (132.18°E, 33.17°N).

influences the propagation of semidiurnal internal tides. The Kuroshio is strong in July with current speeds higher than 1.2 m/s (Fig. 14a), but weak in October with current speeds lower than 0.9 m/s (Fig. 14b). The two different background fields are used in wave front tracing to explore the influence of the Kuroshio strength on the refraction of internal tides. As shown in Fig. 14c, intense Kuroshio in July causes stronger advection effects, resulting in the eastward refraction of the offshore propagating semidiurnal internal tides. Additionally, the wave front becomes wider as it propagates into deep water when compared to that under the weak Kuroshio.

6. Summary

The Bungo Channel is the main gate for water exchange between the Seto Inland Sea and the Pacific Ocean. Based on moored observations and JCOPE-T results, semidiurnal internal tides in the Bungo Channel are investigated in this study. Their characteristics, energetics, and seasonal variation are analyzed. The main conclusions are outlined as follows:

(1) Intense semidiurnal internal tides in the Bungo Channel are captured by moored observations during 2016/07–2016/10, associated with baroclinic velocities of about 0.3 m/s. Their energy shows an obvious spring-neap cycle, which is generally correlated with the local barotropic tidal forcing. By adopting the EOF analysis, it is found that the observed semidiurnal internal tides are mainly dominated by the first two baroclinic modes.

(2) By analyzing the JCOPE-T results, two generation sites of semidiurnal internal tides located at the Hayasui Strait and the shelf break south of the Bungo Channel are identified. The latter makes a major contribution to the observed semidiurnal internal tides. Northward internal tides generated at the shelf break are superposed with those generated at the Hayasui Strait, causing a complex interference pattern in the channel. Additionally, a large amount of internal tidal energy is radiated into the Pacific Ocean from the shelf break.

(3) Several factors influence the temporal variation of semidiurnal internal tides in the Bungo Channel. The intraseasonal variation of semidiurnal internal tides can be modulated by the *Kyucho*. During summer, the occurrence of *Kyucho* leads to the variation of stratification in the channel and therefore affects the energy conversion of internal tides. Seasonal variation of semidiurnal internal tides in the Bungo Channel is determined mainly by seasonally varying stratification; while those generated at the shelf break are under the combined influence of seasonal stratification and background currents. As semidiurnal internal tides propagate southward into the Pacific Ocean from the shelf break, they are refracted due to the spatially varying stratification and background currents. The changes of Kuroshio in path and strength considerably modulate the refraction of southward semidiurnal internal tides.

CRediT authorship contribution statement

Shuya Wang: Conceptualization, Investigation, Methodology, Visualization, Writing – original draft, Writing – review & editing. **Xinyu Guo:** Conceptualization, Funding acquisition, Supervision, Writing – review & editing. **Akihiko Morimoto:** Data curation. **Anzhou**

Cao: Conceptualization, Writing – review & editing. **Eisuke Tsutsumi:** Conceptualization, Validation. **Yasumasa Miyazawa:** Data curation. **Sergey M. Varlamov:** Data curation, Resources.

Declaration of competing interest

The authors declare that they have no known competing financial interests or personal relationships that could have appeared to influence the work reported in this paper.

Data availability

Data will be made available on request.

Acknowledgments

The authors deeply thank the editor and two anonymous reviewers for their constructive suggestions, which greatly improved this paper.

This study was supported by a Grant-in-Aid for Scientific Research (MEXT KAKENHI, grant number: 20H01972, 22H05206). S. Wang thanks the support from JSPS Postdoctoral Fellowships for Research in Japan (grant number: 23KF0056). A. Cao thanks the support from the China Scholarship Council (grant number: 202006325025).

Appendix:. Validation of the JCOPE-T results

The JCOPE-T results are validated by comparison with moored observations. First, Fig. A1 shows the comparison of barotropic tidal currents between JCOPE-T results and moored observations. The meridional component of barotropic tidal currents from JCOPE-T is in good consistency with observations (Fig. A1a), while the zonal one shows some differences from the observations (Fig. A1b). The root-mean-square error (RMSE) and correlation coefficient (r) are 0.03 (0.07) m/s and 0.91 (0.97) for the zonal (meridional) component, respectively.

Second, the results for semidiurnal internal tides from JCOPE-T and observations are presented in Fig. A1c-A1d. On the whole, the JCOPE-T reproduces the observed semidiurnal internal tides in the Bungo Channel. The semidiurnal baroclinic velocities from the JCOPE-T results and observations are in comparable strength and intensified near the surface and bottom regions. Also, both of them exhibit obvious spring-neap cycles and basically coincide with the local tidal forcing. Moreover, temporal variation of the kinetic energy of semidiurnal internal tides from JCOPE-T also agrees with that from observations (Fig. A1e), with RMSE $= 3$ J/m^3 and $r = 0.6$. The appearance of some biases may be attributed to the lack of data assimilation in JCOPE-T in shallow regions.

Moreover, we also compare the JCOPE-T results with observations from another moored ADCP at (132.18°E, 33.17°N), which was deployed in July 2016. Because the observational period only lasted no longer than one month, the data is not shown in the main text for the investigation of internal tides. The results shown in Fig. A2 also suggest good consistency between the JCOPE-T and observations. Hence, based on the above validations, we believe that the JCOPE-T results are reasonable and can be used in corresponding investigations.

References

Alford, M.H., MacKinnon, J.A., Nash, J.D., Simmons, H., Pickering, A., Klymak, J.M., Pinkel, R., Sun, O., Rainville, L., Musgrave, R., Beitzel, T., Fu, K., Lu, C., 2011. Energy Flux and Dissipation in Luzon Strait: Two Tales of Two Ridges. J. Phys. Oceanogr. 41, 2211–2222.
Cacchione, D.A., Pratson, L.F., Ogston, A.S., 2002. The shaping of continental slopes by internal tides. Science 296, 724–727.
Cao, A., Guo, Z., Lv, X., Song, J., Zhang, J., 2017. Coherent and incoherent features, seasonal behaviors and spatial variations of internal tides in the northern South China Sea. J. Mar. Syst. 172, 75–83.
Carter, G.S., Merrifield, M.A., Becker, J.M., Katsumata, K., Gregg, M.C., Luther, D.S., Levine, M.D., Boyd, T.J., Firing, Y.L., 2008. Energetics of M2 Barotropic-to-Baroclinic Tidal Conversion at the Hawaiian Islands. J. Phys. Oceanogr. 38, 2205–2223.
Chang, P., Guo, X., Takeoka, H., 2009. numerical study of the seasonal circulation in the Seto Inland Sea, Japan. J. Oceanogr. 65, 721–736.
Duda, T.F., Lin, Y., Buijsman, M., Newhall, A.E., 2018. Internal Tidal Modal Ray Refraction and Energy Ducting in Baroclinic Gulf Stream Currents. J. Phys. Oceanogr. 48, 1969–1993.
Duda, T.F., Lin, Y., Newhall, A.E., Helfrich, K.R., Lynch, J.F., Zhang, W.G., Lermusiaux, P.F.J., Wilkin, J., 2019. Multiscale multiphysics data-informed modeling for three-dimensional ocean acoustic simulation and prediction. J. Acoust. Soc. Am. 146, 996–2015.
Egbert, G.D., Erofeeva, S.Y., 2002. Efficient inverse modeling of barotropic ocean tides. J. Atmos. Oceanic Tech. 19, 183–204.
Garrett, C., Kunze, E., 2007. Internal tide generation in the deep ocean. Annu. Rev. Fluid Mech. 39, 57–87.
Gerkema, T., Zimmerman, J.T.F., 2008. An introduction to internal waves (p. 207). Royal NIOZ Lecture Notes.
Gerkema, T., Lam, F.P.A., Maas, L.R.M., 2004. Internal tides in the Bay of Biscay: conversion rates and seasonal effects. Deep Sea Res. Part II 51, 2995–3008.
Gill, A.E., 1982. Atmosphere-Ocean Dynamics. Academic Press 662 pp.
Griffiths, S.D., Grimshaw, R.H.J., 2007. Internal Tide Generation at the Continental Shelf Modeled Using a Modal Decomposition: Two-Dimensional Results. J. Phys. Oceanogr. 37, 428–451.
Isobe, A., Guo, X., Takeoka, H., 2010. Hindcast and predictability of sporadic Kuroshio-water intrusion (kyucho in the Bungo Channel) into the shelf and coastal waters. J. Geophys. Res. 115, C04023.
Jithin, A.K., Francis, P.A., Unnikrishnan, A.S., Ramakrishna, S.S.V.S., 2019. Modeling of Internal Tides in the Western Bay of Bengal: Characteristics and Energetics. J. Geophys. Res. Oceans 124, 8720–8746.
Jithin, A.K., Subeesh, M.P., Francis, P.A., Ramakrishna, S.S.V.S., 2020. Intensification of tidally generated internal waves in the north-central Bay of Bengal. Sci. Rep. 10.
Kaneda, A., Takeoka, H., Nagaura, E., Koizumi, Y., 2002. Periodic Intrusion of Cold Water from the Pacific Ocean into the Bottom Layer of the Bungo Channel in Japan. J. Oceanogr. 58, 547–556.
Kang, D., Fringer, O., 2012. Energetics of barotropic and baroclinic tides in the Monterey Bay area. J. Phys. Oceanogr. 42, 272–290.
Kawamura, Y., Hayami, Y., Kohama, T., Kaneda, A., Takeoka, H., 2006. Occasional intensification of semidiurnal internal tide in Bungo Channel Japan. Geophys. Res. Lett. 33.
Kelly, S.M., Jones, N.L., Nash, J.D., Waterhouse, A.F., 2013. The geography of semidiurnal mode-1 internal-tide energy loss. Geophys. Res. Lett. 40, 4689–4693.
Kelly, S.M., Nash, J.D., 2010. Internal-tide generation and destruction by shoaling internal tides. Geophys. Res. Lett. 37, L23611.
Kerry, C.G., Powell, B.S., Carter, G.S., 2014. The Impact of Subtidal Circulation on Internal Tide Generation and Propagation in the Philippine Sea. J. Phys. Oceanogr. 44, 1386–1405.
Klymak, J.M., Simmons, H.L., Braznikov, D., Kelly, S., MacKinnon, J.A., Alford, M.H., et al., 2016. Reflection of linear internal tides from realistic topography: The Tasman continental slope. J. Phys. Oceanogr. 46, 3321–3337.
Kundu, P.K., Cohen, I.M., 2002. Fluid Mechanics, Second Edition. Academic Press, p. 730 pp..
Lee, I.-H., Wang, Y.-H., Yang, Y., Wang, D.-P., 2012. Temporal variability of internal tides in the northeast South China Sea. J. Geophys. Res. 117, C02013.
Li, Y., Gao, Z., Lenschow, D.H., Chen, F., 2010. An improved approach for parameterizing surface layer turbulent transfer coefficients in numerical models. Bound. Layer Meteorol. 137, 153–165.
Lien, R.C., Gregg, M.G., 2001. Observations of turbulence in a tidal beam and across a coastal ridge. J. Geophys. Res. 106, 4575–4591.
Lien, R.C., Sanford, T.B., Jan, S., Chang, M.-H., Ma, B.B., 2013. Internal tides on the East China Sea continental slope. J. Mar. Res. 71, 151–185.
Liu, K., Sun, J., Guo, C., Yang, Y., Yu, W., Wei, Z., 2019. Seasonal and Spatial Variations of the M2 Internal Tide in the Yellow Sea. J. Geophys. Res. Oceans 124, 1115–1138.
Mackinnon, J.A., Gregg, M.C., 2003. Shear and Baroclinic Energy Flux on the Summer New England Shelf. J. Phys. Oceanogr. 33, 1462–1475.
Masunaga, E., Uchiyama, Y., Suzue, Y., Yamazaki, H., 2018. Dynamics of internal tides over a shallow ridge investigated with a high-resolution downscaling regional ocean model. Geophys. Res. Lett. 45, 3550–3558.
Miyazawa, Y., Zhang, R.C., Guo, X., Tamura, H., Ambe, D., Lee, J.S., Okuno, A., Yoshinari, H., Setou, T., Komatsu, K., 2009. Water mass variability in the Western North Pacific detected in a 15-year eddy resolving ocean reanalysis. J. Oceanogr. 65, 737–756.
Morimoto, A., Dong, M., Kameda, M., Shibakawa, T., Hirai, M., Takejiri, K., Guo, X., Takeoka, H., 2022. Enhanced Cross-Shelf Exchange Between the Pacific Ocean and the Bungo Channel, Japan Related to a Heavy Rain Event. Front. Mar. Sci. 9.
Müller, M., 2013. On the space- and time-dependence of barotropic-to-baroclinic tidal energy conversion. Ocean Model. 72, 242–252.
Munk, W., Wunsch, C., 1998. Abyssal recipes II: energetics of tidal and wind mixing. Deep Sea Res. Part I 45, 1977–2010.
Nagai, T., Hibiya, T., 2012. Numerical simulation of tidally induced eddies in the Bungo Channel: A possible role for sporadic Kuroshio-water intrusion (kyucho). J. Oceanogr. 68, 797–806.
Nagai, T., Hibiya, T., 2013. Effects of tidally induced eddies on sporadic Kuroshio-water intrusion (kyucho). J. Oceanogr. 69, 369–377.
Nash, J.D., Alford, M.H., Kunze, E., 2005. Estimating Internal Wave Energy Fluxes in the Ocean. J. Atmos. Oceanic Tech. 22, 1551–1570.

Nash, J.D., Kunze, E., Lee, C.M., Sanford, T.B., 2006. Structure of the Baroclinic Tide Generated at Kaena Ridge Hawaii. J. Phys. Oceanogr. 36, 1123–1135.
Nash, J.D., Alford, M.H., Kunze, E., Martini, K., Kelly, S., 2007. Hotspots of deep ocean mixing on the Oregon continental slope. Geophys. Res. Lett. 34.
Nikurashin, M., Ferrari, R., 2013. Overturning circulation driven by breaking internal waves in the deep ocean. Geophys. Res. Lett. 40, 3133–3137.
Niwa, Y., Hibiya, T., 2011. Estimation of baroclinic tide energy available for deep ocean mixing based on three-dimensional global numerical simulations. J. Oceanogr. 67, 493–502.
Park, J.-H., Farmer, D., 2013. Effects of Kuroshio intrusions on nonlinear internal waves in the South China Sea during winter. J. Geophys. Res. Oceans 118, 7081–7094.
Park, J.-H., Watts, D.R., 2006. Internal tides in the southwestern Japan/East Sea. J. Phys. Oceanogr. 36, 22–34.
Pickering, A., Alford, M., Nash, J., Rainville, L., Buijsman, M., Ko, D.S., Lim, B., 2015. Structure and Variability of Internal Tides in Luzon Strait. J. Phys. Oceanogr. 45, 1574–1594.
Rudnick, D.L., Boyd, T.J., Brainard, R.E., Carter, G.S., Egbert, G.D., Gregg, M.C., Holloway, P.E., Klymak, J.M., Kunze, E., Lee, C.M., Levine, M.D., Luther, D.S., Martin, J.P., Merrifield, M.A., Moum, J.N., Nash, J.D., Pinkel, R., Rainville, L., Sanford, T.B., 2003. From tides to mixing along the Hawaiian ridge. Science 301, 355–357.
Saha, S., Moorthi, S., Pan, H., Wu, X., Wang, J., et al., 2010. The NCEP Climate Forecast System Reanalysis. Bull. Am. Meteorol. Soc. 91, 1015–1057.
Saha, S., Moorthi, S., Wu, X., Wang, J., Nadiga, S., Tripp, P., Behringer, D., Hou, Y.-T., Chuang, H.-Y., Iredell, M., Ek, M., Meng, J., Yang, R., Mendez, M.P., van den Dool, H., Zhang, Q., Wang, W., Chen, M., Becker, E., 2014. The NCEP Climate Forecast System Version 2. J. Clim. 27, 2185–2208.
Simmons, H.L., Hallberg, R.W., Arbic, B.K., 2004. Internal wave generation in a global baroclinic tide model. Deep Sea Res. Part II 51, 3043–3068.
Takeoka, H., Yoshimura, T., 1988. The Kyucho in Uwajima Bay. J. Oceanogr. 44, 6–16.
Takeoka, H., Akiyama, H., Kikuchi, T., 1993. The Kyucho in the Bungo Channel, Japan—Periodic intrusion of oceanic warm water. J. Oceanogr. 49, 369–382.
Tchilibou, M., Koch-Larrouy, A., Barbot, S., Lyard, F., Morel, Y., Jouanno, J., Morrow, R., 2022. Internal tides off the Amazon shelf during two contrasted seasons: interactions with background circulation and SSH imprints. Ocean Sci. 18, 1591–1618.
Tsutsumi, E., Guo, X., 2016. Climatology and linear trends of seasonal water temperature and heat budget in a semienclosed sea connected to the Kuroshio region. J. Geophys. Res. Oceans 121, 4649–4669.
Varlamov, S.M., Guo, X., Miyama, T., Ichikawa, K., Waseda, T., Miyazawa, Y., 2015. M2 baroclinic tide variability modulated by the ocean circulation south of Japan. J. Geophys. Res. Oceans 120, 3681–3710.
Wang, S., Cao, A., Li, Q., Chen, X., 2021. Reflection of K1 Internal Tides at the Continental Slope in the Northern South China Sea. J. Geophys. Res. Oceans 126.
Wang, Z., Li, Q., Wang, C., Qi, F., Duan, H., Xu, J., 2020. Observations of internal tides off the coast of Shandong Peninsula, China. Estuar. Coast. Shelf Sci. 245, 106944.
Waseda, T., Webb, A., Kiyomatsu, K., Fujimoto, W., Miyazawa, Y., Varlamov, S., Horiuchi, K., Fujiwara, T., Taniguchi, T., Matsuda, K., Yoshikawa, J., 2016. Marine energy resource assessment at reconnaissance to feasibility study stages; wave power, ocean and tidal current power, and ocean temperature power. Journal of the Japan Society of Naval Architects and Ocean Engineers 23, 189–198 in Japanese.
Xu, P., Yang, W., Zhu, B., Wei, H., Zhao, L., Nie, H., 2020. Turbulent mixing and vertical nitrate flux induced by the semidiurnal internal tides in the southern Yellow Sea. Cont. Shelf Res. 208, 104240.
Xu, Z., Yin, B., Hou, Y., Xu, Y., 2013. Variability of internal tides and near-inertial waves on the continental slope of the northwestern South China Sea. J. Geophys. Res. Oceans 118.
Xu, Z., Yin, B., Hou, Y., Liu, A.K., 2014. Seasonal variability and north–south asymmetry of internal tides in the deep basin west of the Luzon Strait. J. Mar. Syst. 134, 101–112.
Yu, X., Guo, X., 2018. Intensification of water temperature increase inside the bottom cold water by horizontal heat transport. Cont. Shelf Res. 165, 26–36.
Zhao, Z., Alford, M.H., Girton, J.B., Rainville, L., Simmons, H.L., 2016. Global Observations of Open-Ocean Mode-1 M2 Internal Tides. J. Phys. Oceanogr. 46, 1657–1684.
Zhao, Z., Alford, M.H., MacKinnon, J.A., Pinkel, R., 2010. Long-range propagation of the semidiurnal internal tide from the Hawaiian Ridge. J. Phys. Oceanogr. 40, 713–736.